Letter

Distinguishing dual lattices by strong-pulse matter-wave diffraction

Fangde Liu,[1,*] Wei Han,[1,*] Yunda Li,[1] Feifan Zhao,[1] Liangchao Chen,[1,2] Lianghui Huang,[1,2] Pengjun Wang,[1,2] Zengming Meng,[1,2,†] and Jing Zhang[1,2,‡]

[1]*State Key Laboratory of Quantum Optics Technologies and Devices, Institute of Opto-Electronics, Collaborative Innovation Center of Extreme Optics, Shanxi University, Taiyuan, Shanxi 030006, People's Republic of China*

[2]*Hefei National Laboratory, Hefei, Anhui 230088, People's Republic of China*

(Received 23 July 2025; accepted 19 December 2025; published 13 January 2026)

Dual lattices such as honeycomb and hexagonal lattices typically obey Babinet's principle in optics, which states that the expected interference patterns of two complementary diffracting objects are identical and indistinguishable, except for their overall intensity. Here, we study Kapitza-Dirac diffraction of Bose-Einstein condensates in optical lattices and find that matter waves in dual lattices obey Babinet's principle only under the condition of weak-pulse Raman-Nath regime. In contrast, the Kapitza-Dirac matter-wave diffraction in the strong-pulse Raman-Nath regime, which generates subwavelength phase structures via phase wrapping, can break Babinet's principle and clearly resolve the distinct interference patterns of the dual honeycomb and hexagonal lattices. This method offers exceptional precision in characterizing lattice configurations and advance the study of symmetry-related phenomena, overcoming the limitations of real-space imaging.

DOI: 10.1103/swz7-qnpx

Optical lattices with ultracold atoms offer a well-established experimental platform for quantum simulation of complex strongly interacting many-body systems, owing to the excellent controllability of system parameters and refined measurement techniques [1–3]. A variety of optical lattice geometries can be realized by interfering different sets of laser beams [4,5], including honeycomb [6], hexagonal [7], checkerboard [8], quasihoneycomb [9], kagome [10], and Lieb [11] lattices; superlattices [12,13]; as well as more complex structures such as spin-dependent optical lattices [14–17] and twisted bilayer optical lattices [18]. Among various lattice geometries, honeycomb and hexagonal lattices have attracted significant attention due to their unique symmetries and the rich physics they can support, such as Dirac cones [19], topological edge states [20], and the quantum Hall effect [21].

In addition to the global lattice geometry, a lattice's physical properties are determined by the arrangement of atoms within the unit cell, which in turn gives rise to distinct band dispersions, symmetry representations, and topological characteristics. These intracell degrees of freedom are classified by Wyckoff positions, which define distinct site-symmetry orbits and sublattice arrangements, leading to inequivalent band representations and momentum-space signatures [22,23]. Different occupations of Wyckoff positions on the same Bravais lattice give rise to distinct lattice geometries. For example, on a triangular Bravais lattice, occupying the $1a$, $2b$, and $3c$ Wyckoff positions yields hexagonal, honeycomb, and kagome lattices [24,25], respectively, each exhibiting distinct physical and topological characteristics. However, conventional ultracold-atom measurements, limited by the spatial resolution of *in situ* imaging [26–29], typically cannot resolve intracell distributions, making distinct atomic arrangements within the same lattice structure often experimentally indistinguishable.

Optical lattices can be effectively studied using graph theory, which provides an intuitive framework for analyzing their geometric structures and revealing the underlying topological properties [22,30]. A graph $G(v, e, f)$ is defined as a set of vertices (v), edges (e) and faces (f), where each edge connects two vertices, and the faces represent the enclosed regions formed by these connections. The dual graph $G^*(v^*, e^*, f^*)$ of the graph G, formed by interchanging the roles of faces and vertices in a graph, follow the relations $v^* = f$, $e^* = e$, and $f^* = v$, where edges remain unchanged, and vertices and faces are swapped between the primal and dual graphs. This duality establishes a profound connection between lattice geometries. Notably, honeycomb and hexagonal lattices exemplify this relationship [31,32], as shown in Fig. 1(a). In optics, dual lattices obey Babinet's principle, which states that the interference patterns of two complementary diffracting objects are essentially identical, except for the overall intensity of the diffracted pattern [33,34].

Here, we investigate Kapitza-Dirac diffraction of matter waves in dual honeycomb and hexagonal optical lattices. We find that Babinet's principle holds in the weak-pulse Raman-Nath regime but breaks down in the strong-pulse regime, where the dual lattices exhibit markedly different diffraction patterns in momentum space. This breakdown can be attributed to the phase wrapping induced by a strong pulse in the Raman-Nath regime, which encodes subwavelength real-space phase information within a unit cell into higher-order diffraction peaks in momentum space. These discrete momentum peaks self-organize into distinct diffraction patterns that reflect the different phase wrapping experienced by atoms

*These authors contributed equally to this work.
†Contact author: zmmeng01@sxu.edu.cn
‡Contact author: jzhang74@sxu.edu.cn

 ©2026 American Physical Society

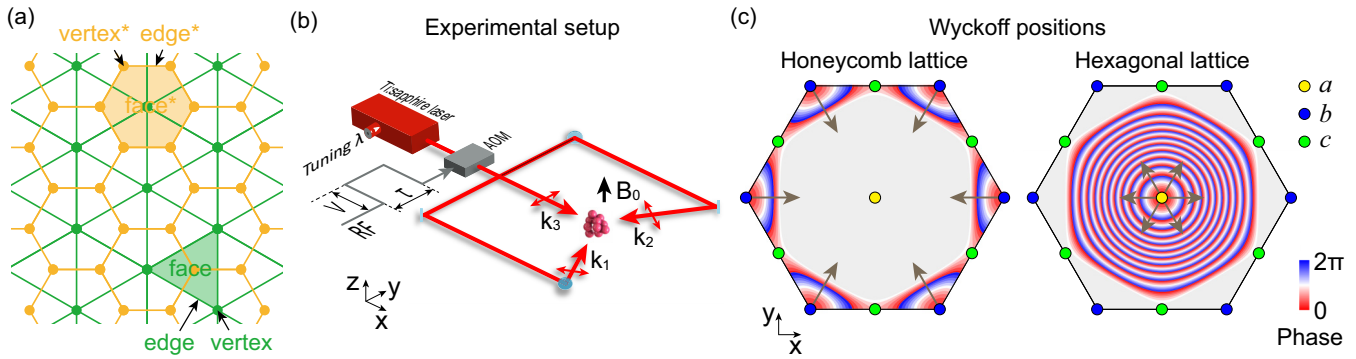

FIG. 1. Dual lattice structures, experimental setup and phase wrapping in the strong-pulse regime. (a) Representation of dual graph for honeycomb and hexagonal lattices. The hexagonal lattice (green) consists of vertices, edges, and faces, while its dual lattice, the honeycomb lattice (yellow), replaces each face of the hexagonal lattice with a vertex and connects vertices where adjacent faces share an edge. (b) Schematic of the experimental setup. Three coplanar lattice beams intersect at 120° in the xy plane with linear p polarizations, while a homogeneous magnetic bias field is applied along the z axis. A Ti:sapphire laser is used to continuously tune the wavelength of the optical lattice. The pulse duration τ and strength V_0 of the lattice beams are controlled by the RF voltage V applied to the acousto-optic modulator (AOM). (c) Phase wrapping of matter wave in the honeycomb and hexagonal lattices under the strong-pulse Raman-Nath regime. Atoms occupy the Wyckoff positions b and a in the honeycomb and hexagonal lattices, respectively. Bottom layers show the contour map of the subwavelength phase structures at $V_0\tau/\hbar = 12 \times 2\pi$. Brown arrows indicate the directions of the steepest gradient of the lattice potential.

at inequivalent Wyckoff positions in the dual lattices. Using time-of-flight imaging, we observe that the diffraction patterns of the honeycomb and hexagonal lattices in the strong-pulse Raman-Nath regime exhibit star-shaped and hexagonal structures, respectively. Furthermore, by manipulating the scalar and vector polarizabilities of the atoms, we demonstrate how to realize various lattice structures, including dual honeycomb and hexagonal lattices, as well as more complex lattices with different symmetries, and how to distinguish them using matter-wave diffraction.

A schematic of the experimental setup is shown in Fig. 1(b). Bose-Einstein condensates (BECs) with up to 5×10^5 rubidium-87 (^{87}Rb) atoms in the spin state $|F = 1, m_F = 1\rangle$ of the ground-state manifold are prepared in a crossed optical dipole trap. We use three laser beams, interfered at angles of 120° in the xy plane, to create a two-dimensional (2D) optical lattice. The polarizations of the lattice beams are linear within the plane of interference and perpendicular to a homogeneous magnetic guiding field of $B_0 = 2.7$ G, which defines the quantization axis along the z direction. The lattice beams are controlled by a single-pass AOM to generate optical lattice pulses. By using a Ti:sapphire laser with a continuously tunable wavelength range of $\triangle\lambda = 46$ nm (774–820 nm), we can flexibly manipulate the scalar and vector polarizabilities of the ac Stark shift, enabling the realization of tunable lattice structures ranging from honeycomb to hexagonal lattices.

The atom-laser electric dipole interaction gives rise to a lattice potential $V(\mathbf{r})$, which consists of a scalar potential $V_s(\mathbf{r})$ and a vector potential $V_v(\mathbf{r})$, and can be written as

$$V(\mathbf{r}) = V_s(\mathbf{r}) + V_v(\mathbf{r}). \tag{1}$$

The scalar potential is $V_s(\mathbf{r}) = -\alpha^{(0)}(\omega, F)|\mathbf{E}|^2$ and the vector potential is $V_v(\mathbf{r}) = -\alpha^{(1)}(\omega, F)(i\mathbf{E}^* \times \mathbf{E}) \cdot \hat{e}_B \frac{m_F}{F}$, where $\alpha^{(0)}(\omega, F)$ and $\alpha^{(1)}(\omega, F)$ denote the scalar and vector polarizabilities, respectively [35]. The unit vector $\hat{e}_B$ indicates the direction of the magnetic quantization axis, and m_F and F are the magnetic and total angular momentum quantum numbers of atoms in a hyperfine ground-state manifold. The optical electric field vector formed by the three laser beams is given by $\mathbf{E} = \sum_{j=1}^{3} E_0 \hat{\epsilon}_j e^{i(\mathbf{k}_j \cdot \mathbf{r} - \omega t)}$ with E_0 denoting the field amplitude, $\hat{\epsilon}_j$ the polarization vector, ω the angular frequency, and $\mathbf{k}_j$ the wave vector of the jth laser beam. For polarization perpendicular to the quantization axis z, the scalar potential is $V_s(\mathbf{r}) = -\alpha^{(0)}(\omega, F)E_0^2[3 - \sum_{j=1}^{3} \cos(\mathbf{b}_j \cdot \mathbf{r})]$ and the vector potential is $V_v(\mathbf{r}) = -\alpha^{(1)}(\omega, F)E_0^2[\sqrt{3}\sum_{j=1}^{3} \sin(\mathbf{b}_j \cdot \mathbf{r})]\frac{m_F}{F}$, where $\mathbf{b}_1 = \mathbf{k}_2 - \mathbf{k}_3$, $\mathbf{b}_2 = \mathbf{k}_3 - \mathbf{k}_1$ and $\mathbf{b}_3 = \mathbf{k}_1 - \mathbf{k}_2$ are the reciprocal lattice vectors. In the case of polarization along the quantization axis z, the vector potential vanishes, leaving only the scalar potential.

The lattice potential $V(\mathbf{r})$ can be effectively controlled by tuning the frequency to change the scalar and vector polarizabilities $\alpha^{(0)}$ and $\alpha^{(1)}$. A pure scalar potential $V_s(\mathbf{r})$ with $\alpha^{(0)} > 0$ (red detuning) forms a honeycomb lattice, whereas $\alpha^{(0)} < 0$ (blue detuning) leads to a hexagonal lattice. A pure vector potential $V_v(\mathbf{r})$ instead gives rise to a triangular lattice (see Fig. S1 in the Supplemental Material [36]). When $\alpha^{(0)} = \pm\alpha^{(1)}\frac{m_F}{F} > 0$, the total lattice potential $V(\mathbf{r})$ forms a hexagonal lattice. Conversely, when $\alpha^{(0)} = \pm\alpha^{(1)}\frac{m_F}{F} < 0$, the lattice potential $V(\mathbf{r})$ forms a honeycomb lattice. The honeycomb and hexagonal lattice potentials, differing only by a sign, constitute a pair of dual lattices [31,32], as illustrated in Fig. 1(a).

To characterize the lattice structure, we use Kapitza-Dirac matter-wave diffraction [10,37]. In the Raman-Nath regime, defined by a short pulse duration $\tau \ll \tau_{\text{lim}} = h/\sqrt{4V_0E_r}$ (with E_r denoting the photon recoil energy, V_0 the lattice depth, and h Planck's constant), the atomic kinetic energy can be neglected [38]. In this regime, the lattice potential $V(\mathbf{r})$ acts as a spatially dependent phase grating on the matter wave, and the evolution of the BEC can be described classically by $\Psi(\mathbf{r}, \tau) = \Psi(\mathbf{r}, 0)e^{iV(\mathbf{r})\tau/\hbar}$, where $\Psi(\mathbf{r}, 0)$ is the initial wave

function. The induced phase modulation scale is directly determined by the product of the lattice depth V_0 and the pulse duration τ. While this modulation is encoded in position space, it can be revealed in momentum space through time-of-flight (TOF) absorption imaging [39]. Outside the Raman-Nath regime ($\tau > \tau_{\mathrm{lim}}$), the atomic kinetic energy becomes significant, rendering the phase grating approximation inadequate for accurately describing the evolution of the BEC. In this regime, the atomic kinetic and potential energies exchange periodically, leading to oscillations of atoms between low-order and high-order diffraction momentum states. Accurate determination of the diffraction dynamics requires the full quantum evolution by solving the Schrödinger equation (see Sec. I in the Supplemental Material [36]).

Furthermore, the Raman-Nath regime can be divided into weak-pulse and strong-pulse regions (see Table 1 in the Supplemental Material [36]). In the weak-pulse Raman-Nath regime, characterized by $V_0\tau_{\mathrm{lim}}/\hbar \lesssim 2\pi$, atoms predominantly populate the zeroth- and first-order diffraction momentum states. In this case, the dominant first-order diffraction peaks reflect the reciprocal lattice vectors, and thus encode the periodicity of the optical lattice. Since the dual honeycomb and hexagonal lattice potentials, differing only by a sign, share the same periodic structure, their diffraction patterns are indistinguishable in this regime. When $V_0\tau_{\mathrm{lim}}/\hbar \gg 2\pi$, the system enters the strong-pulse Raman-Nath regime. By further adjusting the parameters such that $V_0\tau/\hbar > 2\pi$, phase wrapping emerges, leading to a subwavelength periodic modulation imprinted onto the real-space wave function, as shown in Fig. 1(c). This real-space modulation is encoded in the momentum distribution through the appearance of higher-order diffraction peaks. The accessible diffraction order is determined by the local gradient of the lattice potential experienced by the atoms. A steep gradient at the atomic position leads to more rapid spatial phase variation, thereby enabling diffraction into higher-order momentum states through enhanced phase wrapping. The spatial variation of the potential gradient within a primitive cell encodes the fine structure of the lattice potential into the momentum-space diffraction pattern via this phase-wrapping mechanism. For the honeycomb lattice, atoms occupy the Wyckoff position b, where the steepest gradients of the lattice potential predominantly align along six specific directions, as indicated by the arrows in the left panel of Fig. 1(c). Consequently, high-order momentum states are accessible exclusively along these six directions, and a characteristic star-shaped diffraction pattern is expected. In contrast, for the hexagonal lattice, atoms occupy the Wyckoff position a, around which the lattice potential gradient exhibits continuous rotational symmetry, as indicated by the arrows in the right panel of Fig. 1(c). This symmetry results in diffraction with uniform intensity in all directions, and a regular hexagonal diffraction pattern is expected. In Babinet-type optical diffraction scenarios, where complementary apertures or transmission patterns are compared through their far-field intensities, the diffraction patterns of the dual honeycomb and hexagonal lattices are typically indistinguishable.

In the experiment, we apply a lattice potential pulse to the BEC in the hyperfine spin state $|1, 1\rangle$ for a duration τ. Immediately after the pulse, the optical dipole trap is turned off, and the atoms undergo 12 ms of ballistic expansion before being detected via TOF absorption imaging. We first observe atomic diffraction from the dual lattices with a weak pulse. For pulse durations τ within the Raman-Nath regime, no phase wrapping occurs, and diffraction predominantly occurs at the first-order momentum components $\pm\mathbf{b}_i$ ($i = 1, 2, 3$). In this regime, the dual honeycomb and hexagonal lattices are indistinguishable in their momentum diffraction patterns, as shown in Figs. 2(a)–2(b) and 2(d)–2(e). For pulse durations τ outside the Raman-Nath regime, while the diffraction remains primarily at first-order momenta, the system exhibits a periodic exchange between kinetic and potential energy, leading to oscillations of atomic populations between the zeroth- and first-order diffraction momentum states, as illustrated in Figs. 2(c) and 2(f). Even in this regime, the diffraction dynamics of the dual lattices remain nearly identical and indistinguishable aside from a difference in average atom number. Consequently, in the weak-pulse regime, the momentum diffraction of the dual lattices follows Babinet's principle.

We then observe atomic diffraction from the dual lattices by fixing the pulse duration τ within the Raman-Nath regime and varying the lattice depth from weak to strong pulses. At a relatively weak lattice depth and under the condition $V_0\tau/\hbar \ll 2\pi$, the resulting diffraction patterns are nearly identical for the honeycomb and hexagonal lattices, making them difficult to distinguish, as shown in the first column of Figs. 3(b) and 3(d). As the lattice depth increases toward $V_0\tau/\hbar \simeq 2\pi$, phase wrapping gradually emerges, the diffraction patterns formed by higher-order momentum states begin to diverge between the honeycomb and hexagonal lattices, as shown in the second column of Figs. 3(b) and 3(d). In the strong-pulse regime and under the condition $V_0\tau/\hbar \gg 2\pi$, phase wrapping becomes more pronounced, as illustrated in Figs. 3(a) and 3(c). The subwavelength phase information is encoded in higher-order diffraction momentum components. Due to atoms occupying different Wyckoff positions in the dual lattices, they experience distinct local phase gradients and wrapping effects. As a result, the diffraction patterns become clearly distinguishable. This is evident in the third column of Figs. 3(b) and 3(d), where the honeycomb lattice produces a star-shaped pattern due to sharp potential gradients along six discrete directions, while the hexagonal lattice yields a regular hexagonal pattern due to the continuous rotational symmetry of the potential gradients around the atomic Wyckoff position. The experimental results, obtained from TOF absorption images [first row of Figs. 3(b) and 3(d)], are in excellent agreement with numerical simulations based on the full quantum evolution of the BEC [second row of Figs. 3(b) and 3(d)].

The emergence of phase wrapping in the strong-pulse Raman-Nath regime sheds light on the intrinsic structure and symmetry distinctions of the dual lattices. Matter-wave diffraction in the strong-pulse Raman-Nath regime breaks Babinet's principle, enabling clear resolution of the dual lattice structures in momentum space. Such a distinction is challenging to achieve within Babinet-type optical diffraction, where the far-field intensity patterns of complementary structures are typically indistinguishable. It is worth noting that phase wrapping has also proved highly effective in revealing underlying structural and dynamical properties, and

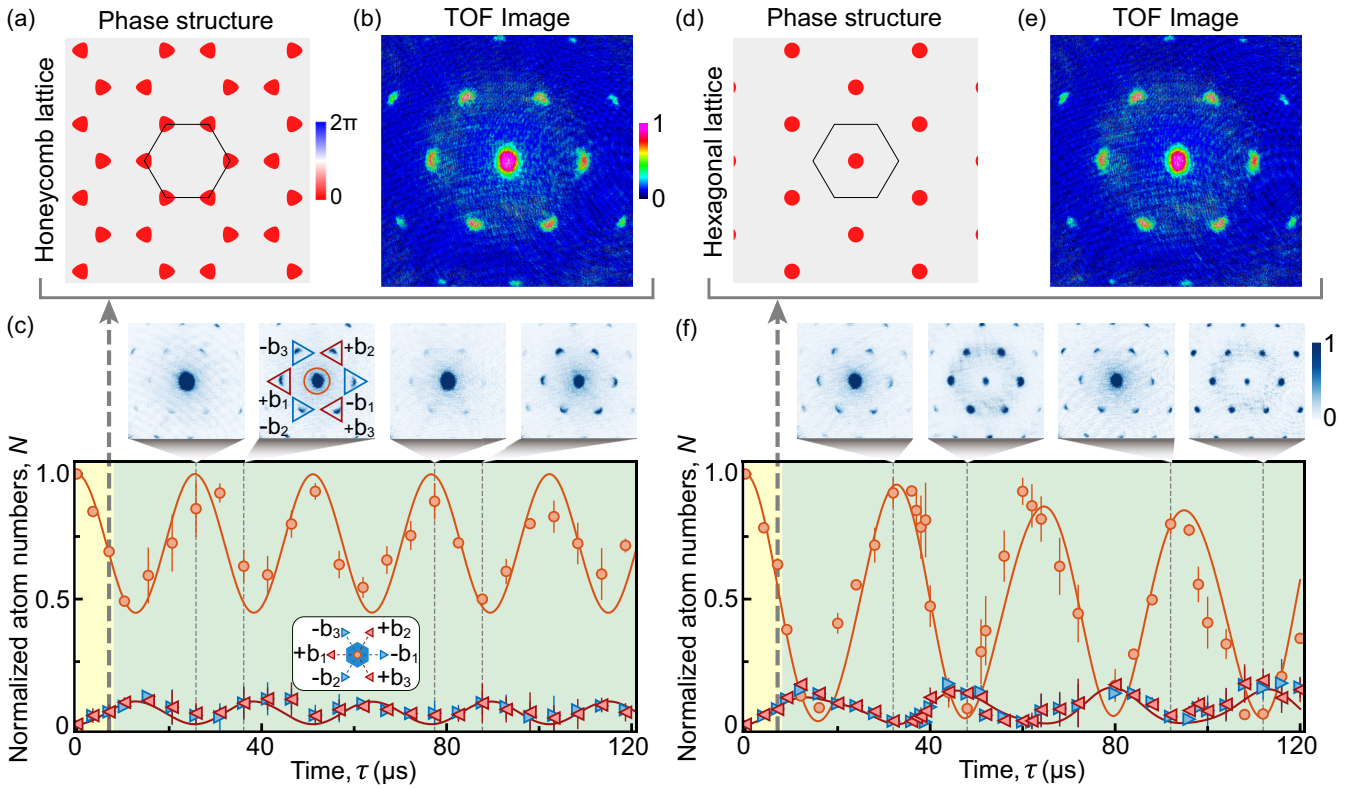

FIG. 2. Kapitza-Dirac diffraction of a BEC in dual lattices under weak-pulse conditions obeying Babinet's principle. (a)–(c) correspond to the honeycomb lattice; (d)–(f) to the hexagonal lattice. (a), (d) Phase structures near the atomic Wyckoff positions at $V_0\tau/\hbar = 0.6 \times 2\pi$. (b), (e) TOF images of Kapitza-Dirac diffraction under a weak pulse ($\tau = 7$ μs) in the Raman-Nath regime. (c), (f) Time evolution of normalized atomic populations in different momentum components. Insets show TOF images at various pulse durations. Orange circles and lines denote the zero-momentum component; red (blue) triangles and lines correspond to the first-order diffraction components at $+\mathbf{b}_{1,2,3}$ ($-\mathbf{b}_{1,2,3}$). Yellow- and green-shaded regions indicate the Raman-Nath and non-Raman-Nath regimes, respectively. The lattice depth is fixed at $V_0 = 23\,E_r$.

is widely applied in fields such as structural reconstruction [40–43].

By tuning the wavelength of the lattice beams to adjust the polarizability ratio $\alpha = \alpha^{(0)}/\alpha^{(1)}$ of the atoms in the $|1, 1\rangle$ state, we can achieve continuous control over the lattice structure, as shown in Fig. 4(a). When $\alpha = 1$ and $\alpha = -1$, the system realizes a hexagonal lattice and a honeycomb lattice, respectively, both exhibiting C_6 rotational symmetry. When $\alpha \neq \pm 1$, the lattice retains only C_3 rotational symmetry. The reduction of the lattice rotational symmetry from C_6 to C_3 directly leads to the opening of an energy gap at the Dirac point, enabling topological control over the energy band structure (see Fig. S2 in the Supplemental Material [36]). To identify the resulting lattice geometry, we introduce the asymmetry parameter S [44], defined as $S = \frac{\sum_i (P_{\mathbf{b}_i} - P_{-\mathbf{b}_i})}{\sum_i (P_{\mathbf{b}_i} + P_{-\mathbf{b}_i})}$, where $P_{\mathbf{b}_i}$ and $P_{-\mathbf{b}_i}$ are the normalized atomic populations in the first-order diffraction peaks at $+\mathbf{b}_i$ and $-\mathbf{b}_i$, respectively. For a weak pulse with a duration of $\tau = 12$ μs, the asymmetry parameter S as a function of the wavelength is shown in Fig. 4(b), where $S = 0$ precisely identifies the positions of the hexagonal and honeycomb lattices at $\lambda_1 = 787.54$ nm and $\lambda_2 = 792.48$ nm, respectively. It is also found that while the time evolution of atomic populations at the first-order diffraction momenta $\pm\mathbf{b}_i$ is synchronized (with $S = 0$) in the hexagonal and honeycomb lattices with C_6 rotational symmetry, the populations at $+\mathbf{b}_i$ and $-\mathbf{b}_i$ exhibit unsynchronized oscillations in lattices with C_3 rotational symmetry, as shown in Figs. 4(c) and 4(d).

In conclusion, we demonstrate that Kapitza-Dirac matter-wave diffraction in the strong-pulse Raman-Nath regime breaks Babinet's principle and enables the clear resolution of dual honeycomb and hexagonal lattices in momentum space. By contrast, in the weak-pulse Raman-Nath regime, the diffraction patterns of the dual lattices remain indistinguishable, consistent with Babinet's principle. The strong-pulse Raman-Nath regime induces phase wrapping of the matter wave, which encodes real-space subwavelength phase information within a unit cell into higher-order diffraction peaks in momentum space. Atoms occupying distinct Wyckoff positions in the dual lattices experience fundamentally different phase wrapping, resulting in clearly distinguishable diffraction patterns. While the honeycomb lattice yields a star-shaped diffraction pattern, the hexagonal lattice displays a regular hexagonal pattern. By precisely adjusting the scalar and vector polarizabilities of the atoms, we achieve controllable transitions among honeycomb, hexagonal, and C_3 rotationally symmetric lattice geometries.

In addition to distinguishing specific dual lattices, our approach provides a general framework for probing the intracell structure in arbitrary optical lattices. By extracting subwavelength phase information revealed by strong-pulse matter-wave diffraction patterns, we can resolve the

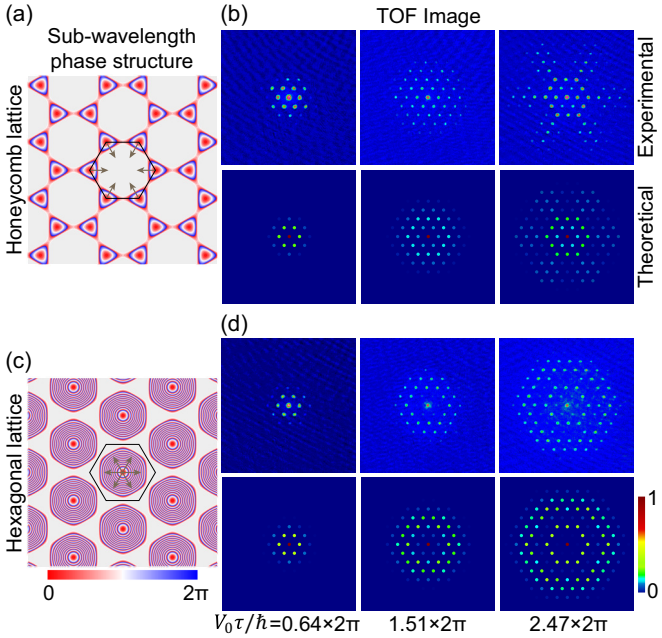

FIG. 3. Breaking of Babinet's principle via phase-wrapped matter-wave diffraction in dual lattices. Panels (a) and (b) correspond to the honeycomb lattice, (c) and (d) to the hexagonal lattice. (a), (c) Phase wrapping near the atomic Wyckoff positions at $V_0\tau/\hbar = 12\times 2\pi$. (b), (d) Kapitza-Dirac diffraction patterns as a function of pulse strength V_0 at a fixed pulse duration of $\tau = 7$ μs in the Raman-Nath regime. The upper panels show experimental results; the lower panels present theoretical predictions. From left to right, the pulse strengths are $V_0 = 25E_r$, $59E_r$, and $95E_r$, corresponding to phase wrapping parameters of $V_0\tau/\hbar = 0.64\times 2\pi$, $1.51\times 2\pi$, and $2.47\times 2\pi$, respectively.

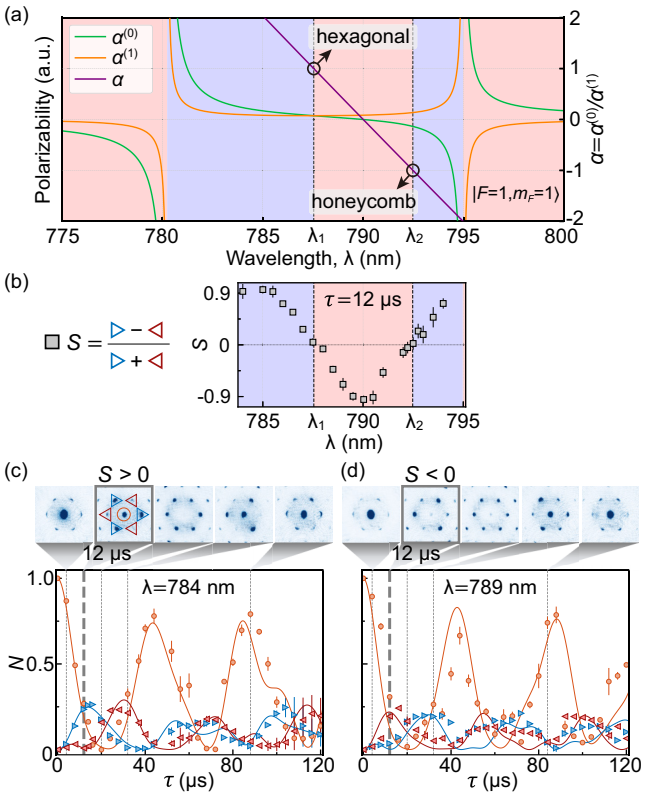

FIG. 4. Continuous control of lattice geometry and diffraction symmetry via laser wavelength. (a) Polarizability of ^{87}Rb atoms in the hyperfine ground state $|F = 1, m_F = 1\rangle$ as a function of wavelength. The ratios of scalar to vector polarizability, with $\alpha = 1$ at $\lambda_1 = 787.54$ nm and $\alpha = -1$ at $\lambda_2 = 792.48$ nm, correspond to the hexagonal and honeycomb lattices, respectively. (b) Asymmetry parameter S as a function of wavelength under a weak pulse ($\tau = 12$ μs). The region with $S > 0$ is shaded blue and that with $S < 0$ is shaded pink in (a) and (b). (c),(d) Time evolution of normalized atomic populations in different momentum components during Kapitza-Dirac diffraction for the C_3 rotational symmetry lattice, with $\lambda = 784$ nm in (c) and $\lambda = 789$ nm in (d). The insets show the TOF images at various pulse durations. The lattice depth is fixed at $V_0 = 23E_r$.

occupation of distinct Wyckoff positions within a unit cell. The strong-pulse matter-wave diffraction is highly sensitive to intracell phase variations, enabling the detection of hidden symmetry breaking and Wyckoff-position-dependent phase wrapping beyond the reach of conventional imaging. Such capability naturally extends to diverse lattice geometries, including square, kagome and quasiperiodic lattices, offering a versatile means to reveal subtle symmetry features and fine structural details in optical lattice systems. Furthermore, the force landscape revealed by the diffraction pattern enables our technique to probe the nonequilibrium dynamics of the atomic ensemble. This work establishes strong-pulse Kapitza-Dirac diffraction as a sensitive probe that reveals unique momentum-space fingerprints of the underlying lattice fine structure, offering new opportunities for precision lattice characterization and engineering in ultracold atomic systems.

This research is supported by the National Key Research and Development Program of China (Grants No. 2022YFA1404101 and No. 2021YFA1401700), the Quantum Science and Technology–National Science and Technology Major Project (Grant No. 2021ZD0302003), the National Natural Science Foundation of China (Grants No. 12488301, No. 12034011, No. U23A6004, No. 92476001, No. 92576205, No. 12322409, No. 12474252, No. 12474266, No. 12374245, and No. 12504336), and Tencent (Xplorer Prize).

Data availability. The data that support the findings of this study are available within this Letter and its Supplemental Material [36].

[1] I. Bloch, J. Dalibard, and W. Zwerger, Many-body physics with ultracold gases, Rev. Mod. Phys. **80**, 885 (2008).

[2] I. Bloch, J. Dalibard, and S. Nascimbène, Quantum simulations with ultracold quantum gases, Nat. Phys. **8**, 267 (2012).

[3] M. Lewenstein, A. Sanpera, and V. Ahufinger, *Ultracold Atoms in Optical Lattices: Simulating Quantum Many-Body Systems* (Oxford University Press, Oxford, 2012).

[4] P. Windpassinger and K. Sengstock, Engineering novel optical lattices, Rep. Prog. Phys. **76**, 086401 (2013).

[5] F. Schäfer, T. Fukuhara, S. Sugawa, Y. Takasu, and Y. Takahashi, Tools for quantum simulation with ultracold atoms in optical lattices, Nat. Rev. Phys. **2**, 411 (2020).

[6] C. D. Brown, S. Chang, M. N. Schwarz, T. H. Leung, V. Kozii, A. Avdoshkin, J. E. Moore, and D. Stamper-Kurn, Direct geometric probe of singularities in band structure, Science **377**, 1319 (2022).

[7] J. Struck, C. Ölschläger, R. Le Targat, P. Soltan-Panahi, A. Eckardt, M. Lewenstein, P. Windpassinger, and K. Sengstock, Quantum simulation of frustrated classical magnetism in triangular optical lattices, Science **333**, 996 (2011).

[8] J. Sebby-Strabley, M. Anderlini, P. S. Jessen, and J. V. Porto, Lattice of double wells for manipulating pairs of cold atoms, Phys. Rev. A **73**, 033605 (2006).

[9] L. Tarruell, D. Greif, T. Uehlinger, G. Jotzu, and T. Esslinger, Creating, moving and merging Dirac points with a Fermi gas in a tunable honeycomb lattice, Nature (London) **483**, 302 (2012).

[10] G. B. Jo, J. Guzman, C. K. Thomas, P. Hosur, A. Vishwanath, and D. M. Stamper-Kurn, Ultracold atoms in a tunable optical kagome lattice, Phys. Rev. Lett. **108**, 045305 (2012).

[11] S. Taie, H. Ozawa, T. Ichinose, T. Nishio, S. Nakajima, and Y. Takahashi, Coherent driving and freezing of bosonic matter wave in an optical Lieb lattice, Sci. Adv. **1**, e1500854 (2015).

[12] B. Yang, H. Sun, C. Huang, H. Wang, Y. Deng, H. Dai, Z. Yuan, and J. Pan, Cooling and entangling ultracold atoms in optical lattices, Science **369**, 550 (2020).

[13] M. N. Kosch, L. Asteria, H. P. Zahn, K. Sengstock, and C. Weitenberg, Multifrequency optical lattice for dynamic lattice-geometry control, Phys. Rev. Res. **4**, 043083 (2022).

[14] O. Mandel, M. Greiner, A. Widera, T. Rom, T. W. Hänsch, and I. Bloch, Coherent transport of neutral atoms in spin-dependent optical lattice potentials, Phys. Rev. Lett. **91**, 010407 (2003).

[15] P. Soltan-Panahi, J. Struck, P. Hauke, A. Bick, W. Plenkers, G. Meineke, C. Becker, P. Windpassinger, M. Lewenstein, and K. Sengstock, Multi-component quantum gases in spin-dependent hexagonal lattices, Nat. Phys. **7**, 434 (2011).

[16] P. Soltan-Panahi, D. S. Lühmann, J. Struck, P. Windpassinger, and K. Sengstock, Quantum phase transition to unconventional multi-orbital superfluidity in optical lattices, Nat. Phys. **8**, 71 (2012).

[17] K. Wen, Z. Meng, L. Wang, L. Chen, L. Huang, P. Wang, and J. Zhang, Experimental study of tune-out wavelengths for spin-dependent optical lattice in ^{87}Rb Bose–Einstein condensation, J. Opt. Soc. Am. B **38**, 3269 (2021).

[18] Z. Meng, L. Wang, W. Han, F. Liu, K. Wen, C. Gao, P. Wang, C. Chin, and J. Zhang, Atomic Bose-Einstein condensate in twisted-bilayer optical lattices, Nature (London) **615**, 231 (2023).

[19] N. Fläschner, D. Vogel, M. Tarnowski, B. S. Rem, D. S. Lühmann, M. Heyl, J. C. Budich, L. Mathey, K. Sengstock, and C. Weitenberg, Observation of dynamical vortices after quenches in a system with topology, Nat. Phys. **14**, 265 (2018).

[20] C. Braun, R. Saint-Jalm, A. Hesse, J. Arceri, I. Bloch, and M. Aidelsburger, Real-space detection and manipulation of topological edge modes with ultracold atoms, Nat. Phys. **20**, 1306 (2024).

[21] S. Miao, Z. Zhang, Y. Zhao, Z. Zhao, H. Wang, and J. Hu, Bosonic fractional quantum Hall conductance in shaken honeycomb optical lattices without flat bands, Phys. Rev. B **106**, 054310 (2022).

[22] B. Bradlyn, L. Elcoro, J. Cano, M. G. Vergniory, Z. Wang, C. Felser, M. I. Aroyo, and B. A. Bernevig, Topological quantum chemistry, Nature (London) **547**, 298 (2017).

[23] V. Peri, Z.-D. Song, M. Serra-Garcia, P. Engeler, R. Queiroz, X. Huang, W. Deng, Z. Liu, B. A. Bernevig, and S. D. Huber, Experimental characterization of fragile topology in an acoustic metamaterial, Science **367**, 797 (2020).

[24] J. Cano, B. Bradlyn, Z. Wang, L. Elcoro, M. G. Vergniory, C. Felser, M. I. Aroyo, and B. A. Bernevig, Building blocks of topological quantum chemistry: Elementary band representations, Phys. Rev. B **97**, 035139 (2018).

[25] S. Liu, A. Vishwanath, and E. Khalaf, Shift insulators: Rotation-protected two-dimensional topological crystalline insulators, Phys. Rev. X **9**, 031003 (2019).

[26] W. S. Bakr, J. I. Gillen, A. Peng, S. Fölling, and M. Greiner, A quantum gas microscope for detecting single atoms in a Hubbard-regime optical lattice, Nature (London) **462**, 74 (2009).

[27] J. F. Sherson, C. Weitenberg, M. Endres, M. Cheneau, I. Bloch, and S. Kuhr, Single-atom-resolved fluorescence imaging of an atomic Mott insulator, Nature (London) **467**, 68 (2010).

[28] C. Gross and I. Bloch, Quantum simulations with ultracold atoms in optical lattices, Science **357**, 995 (2017).

[29] M. McDonald, J. Trisnadi, K.-X. Yao, and C. Chin, Superresolution microscopy of cold atoms in an optical lattice, Phys. Rev. X **9**, 021001 (2019).

[30] J. W. Essam and M. E. Fisher, Some basic definitions in graph theory, Rev. Mod. Phys. **42**, 272 (1970).

[31] J. Alicea, O. I. Motrunich, M. Hermele, and M. P. A. Fisher, Criticality in quantum triangular antiferromagnets via fermionized vortices, Phys. Rev. B **72**, 064407 (2005).

[32] O. Ori, F. Cataldo, and M. V. Putz, Topological anisotropy of Stone-Wales waves in graphenic fragments, Int. J. Mol. Sci. **12**, 7934 (2011).

[33] E. Hecht, *Optics* (Pearson Education, London, 2001).

[34] M. Born and E. Wolf, *Principles of Optics* (Cambridge University Press, Cambridge, 1999).

[35] D. Steck, Quantum and Atom Optics, https://atomoptics.uoregon.edu/∼dsteck/teaching/quantum-optics/ (unpublished).

[36] See Supplemental Material at http://link.aps.org/supplemental/10.1103/swz7-qnpx for a detailed description of the theoretical modeling of diffraction dynamics, the experimental setup and lattice preparation, energy band structures and phase-wrapping effects, ^{87}Rb atomic polarizabilities in the hyperfine ground state $|F = 2, m_F = 2\rangle$, and a comparison between Bragg and Kapitza-Dirac diffraction, which includes Ref. [17].

[37] P. L. Gould, G. A. Ruff, and D. E. Pritchard, Diffraction of atoms by light: The near-resonant Kapitza-Dirac effect, Phys. Rev. Lett. **56**, 827 (1986).

[38] Y. B. Ovchinnikov, J. H. Müller, M. R. Doery, E. J. D. Vredenbregt, K. Helmerson, S. L. Rolston, and W. D. Phillips, Diffraction of a released Bose-Einstein condensate by a pulsed standing light wave, Phys. Rev. Lett. **83**, 284 (1999).

[39] K. Wen, Z. Meng, P. Wang, L. Wang, L. Chen, L. Huang, L. Zhou, X. Cui, and J. Zhang, Observation of sub-wavelength phase structure of matter wave with two-dimensional optical lattice by Kapitza-Dirac diffraction, Sci. Rep. **10**, 5870 (2020).

[40] D. C. Ghiglia and M. D. Pritt, *Two-Dimensional Phase Unwrapping: Theory, Algorithms, and Software* (Wiley-Interscience, New York, 1998).

[41] X. Huang, R. Harder, G. Xiong, X. Shi, and I. Robinson, Propagation uniqueness in three-dimensional coherent diffractive imaging, Phys. Rev. B **83**, 224109 (2011).

[42] M. C. Newton, R. Harder, X. Huang, G. Xiong, and I. K. Robinson, Phase retrieval of diffraction from highly strained crystals, Phys. Rev. B **82**, 165436 (2010).

[43] T. Ramos, B. E. Grønager, M. S. Andersen, and J. W. Andreasen, Direct three-dimensional tomographic reconstruction and phase retrieval of far-field coherent diffraction patterns, Phys. Rev. A **99**, 023801 (2019).

[44] C. K. Thomas, T. H. Barter, T. H. Leung, S. Daiss, and D. M. Stamper-Kurn, Signatures of spatial inversion asymmetry of an optical lattice observed in matter-wave diffraction, Phys. Rev. A **93**, 063613 (2016).